

A Polarimetric Radar Analysis of Ice Microphysical Processes in Melting Layers of Winter Storms Using S-Band Quasi-Vertical Profiles

ERICA M. GRIFFIN, TERRY J. SCHUUR, AND ALEXANDER V. RYZHKOV

Cooperative Institute for Mesoscale Meteorological Studies, and NOAA/OAR National Severe Storms Laboratory, and School of Meteorology, University of Oklahoma, Norman, Oklahoma

(Manuscript received 30 May 2019, in final form 22 January 2020)

ABSTRACT

Quasi-vertical profiles (QVPs) obtained from a database of U.S. WSR-88D data are used to document polarimetric characteristics of the melting layer (ML) in cold-season storms with high vertical resolution and accuracy. A polarimetric technique to define the top and bottom of the ML is first introduced. Using the QVPs, statistical relationships are developed to gain insight into the evolution of microphysical processes above, within, and below the ML, leading to a statistical polarimetric model of the ML that reveals characteristics that reflectivity data alone are not able to provide, particularly in regions of weak reflectivity factor at horizontal polarization Z_H . QVP ML statistics are examined for two regimes in the ML data: $Z_H \geq 20$ dBZ and $Z_H < 20$ dBZ. Regions of $Z_H \geq 20$ dBZ indicate locations of MLs collocated with enhanced differential reflectivity Z_{DR} and reduced copolar correlation coefficient ρ_{hv} , while for $Z_H < 20$ dBZ a well-defined ML is difficult to discern using Z_H alone. Evidence of large Z_{DR} up to 4 dB, backscatter differential phase δ up to 8°, and low ρ_{hv} down to 0.80 associated with lower Z_H (from -10 to 20 dBZ) in the ML is observed when pristine, nonaggregated ice falls through it. Positive correlation is documented between maximum specific differential phase K_{DP} and maximum Z_H in the ML; these are the first QVP observations of K_{DP} in MLs documented at S band. Negative correlation occurs between minimum ρ_{hv} in the ML and ML depth and between minimum ρ_{hv} in the ML and the corresponding enhancement of Z_H ($\Delta Z_H = Z_{Hmax} - Z_{Hrain}$).

1. Introduction

Winter precipitation events, particularly transitional storms (e.g., Stewart 1992) and heavy snow, are difficult to accurately forecast and nowcast, largely due to poor parameterization of ice microphysical processes in numerical weather prediction (NWP) models (e.g., Garvert et al. 2005; Lin and Colle 2009; Stark et al. 2013). Since snow and ice particles are typically nonspherical and have aspect ratios, orientations, and bulk densities that vary significantly in clouds both temporally and spatially, polarimetry is a valuable tool that can be used to estimate bulk properties of storms (Ryzhkov et al. 1998). The most pronounced and persistent polarimetric signatures in stratiform clouds are typically those associated with the melting layer (ML) and the dendritic growth layer (DGL—between -10° and -20°C ; e.g., Moisseev et al. 2009; Kennedy and Rutledge 2011; Bechini et al. 2013; Andrić et al. 2013; Griffin et al. 2014, 2018; Schrom et al. 2015; Kumjian and Lombardo 2017).

Ice microphysical processes are particularly complex within and near MLs and are not completely understood, resulting in poor representation of ML microphysics in numerical models. MLs are identified by a narrow, nearly horizontal layer beneath the 0°C isotherm that is typically characterized by high radar reflectivity Z_H , reduced copolar correlation coefficient ρ_{hv} , and increased differential reflectivity Z_{DR} as particles melt (e.g., Byers and Coons 1947; Stewart et al. 1984; Illingworth and Caylor 1989; Zrnić et al. 1993; Fabry and Zawadzki 1995; Gourley and Calvert 2003; Brandes and Ikeda 2004; Tabary et al. 2006; Wolfensberger et al. 2015). Developing a thorough understanding of the polarimetric properties of the ML is important for several reasons. First, the microphysical structure of the ML mirrors key microphysical processes of precipitation formation and evolution aloft and is also closely related to rain drop size distributions below the ML (e.g., Wolfensberger et al. 2015; Kumjian et al. 2016; Trömel et al. 2014, 2017, 2019). Second, current NWP models do not adequately treat melting of snow within the ML, and, third, satellite retrievals require an appropriate microphysical model of

Corresponding author: Erica M. Griffin, erica.griffin@noaa.gov

DOI: 10.1175/JAMC-D-19-0128.1

© 2020 American Meteorological Society. For information regarding reuse of this content and general copyright information, consult the [AMS Copyright Policy](https://www.ametsoc.org/PUBSReuseLicenses) (www.ametsoc.org/PUBSReuseLicenses).

the ML that does not exist. Ideally, all existing models and retrievals should be optimized using vertical profiles of polarimetric radar variables after converting their outputs to the fields of radar variables. These issues all point to the importance of obtaining a catalogue of polarimetric signatures in the ML against which model outputs and satellite retrievals can be compared.

Another important application of improved ML observations is to mitigate “bright band” contamination in quantitative precipitation estimation (QPE) estimates at large distances from the radar, where the radar’s beam intersects mixed-phase and frozen particles within the ML resulting in erroneous rainfall estimates (Giangrande et al. 2008). Techniques that use vertical profiles of reflectivity (VPR) to mitigate ML contamination in QPE have been developed and used with limited success (e.g., Fabry and Zawadzki 1995). More recently, there have been efforts to augment the use of Z_H in VPRs by complementing it with Z_{DR} and ρ_{hv} in a scheme referred to as polarimetric vertical profiles of rain (PVPR; e.g., Matrosov et al. 2007; Kirstetter et al. 2013; Trömel et al. 2017, 2019).

While relatively few studies have documented the polarimetric characteristics of MLs (e.g., Trömel et al. 2014, 2017, 2019; Kumjian et al. 2016; Carlin and Ryzhkov 2019), several (e.g., Brandes and Ikeda 2004; Tabary et al. 2006; Giangrande et al. 2008; Matrosov et al. 2007; Boodoo et al. 2010; Kalogiros et al. 2013; Wolfensberger et al. 2015) have proposed algorithms to automatically detect either the height of the 0°C level or top and bottom of the ML in polarimetric PPIs or RHIs using different combinations and thresholds of ρ_{hv} , Z_{DR} , and Z_H . For example, Wolfensberger et al. (2015) developed an algorithm to detect the ML in stratiform precipitation using polarimetric X-band RHI scans. Their results indicated strong relationships between ML depth and the presence of rimed particles, the vertical velocity of particles, and ML intensity.

More recently, polarimetric quasi-vertical profiles (QVPs; used in this study and described in more detail in section 2) have been used to study ice microphysical processes and document their temporal evolution. The QVP methodology was first implemented by Kumjian et al. (2013) to investigate polarimetric characteristics of refreezing signatures in winter storms and Trömel et al. (2014) to document the reliability of measurements of backscatter differential phase δ in the ML. Ryzhkov et al. (2016) more formally developed the QVP methodology and documented its many benefits, including its abilities to continuously monitor the evolution of the ML and DGL with high vertical resolution, to easily compare data from polarimetric WSR-88D instruments to data from vertically looking remote sensors (e.g., wind profilers, lidars, and cloud radars), and to potentially discriminate between

rimed and aggregated snow. Since then, QVPs have been used by several researchers (e.g., Kumjian and Lombardo 2017; Tobin and Kumjian 2017; Griffin et al. 2018) to study the microphysical structure of stratiform clouds.

Perhaps most relevant to this study is the study of Trömel et al. (2017, 2019), who used QVPs to develop polarimetric rainfall estimation algorithms. To gain insight into microphysics within and above the ML, Trömel et al. (2019) followed the ML detection method of Wolfensberger et al. (2015) to conduct a study that examined X-band polarimetric radar data from 52 stratiform events in Bonn, Germany (BoXPOL). QVPs were used to estimate Z_H , Z_{DR} , ρ_{hv} , and K_{DP} in the ML and DGL at X band. They were also the first to document K_{DP} statistics in the ML at X band. K_{DP} is a particularly valuable polarimetric variable since it contains important information about ice microphysics and is especially useful for the quantification of ice (e.g., Ryzhkov et al. 1998; Griffin et al. 2018; Ryzhkov et al. 2018). It also more accurately characterizes precipitation flux in the ML than either Z_H or Z_{DR} , which are both heavily weighted by large wet snow aggregates (e.g., Trömel et al. 2017, 2019). Since there is often a notable contribution of δ to the total differential phase Φ_{DP} in the ML at S band, Griffin et al. (2018) introduced a method to remove δ contamination in the estimation of K_{DP} . Currently, more statistics are needed to understand the behavior of K_{DP} in the ML and its relation to ice processes aloft and precipitation rates at the surface.

Since January of 2013, we have compiled a database that consists of thousands of hours of polarimetric WSR-88D S-band radar observations in a wide variety of winter precipitation events. Many of those datasets exhibit several intriguing and repetitive polarimetric signatures. In this study, we use QVPs produced from 33 WSR-88D datasets collected during 17 winter weather events to investigate the microphysical evolution and significance of some of those signatures and to improve understanding of the structure and behavior of the ML in cold-season precipitation. Radar data and their microphysical interpretation are presented in context of the thermodynamic environment, provided by the operational 3-km High-Resolution Rapid Refresh (HRRR; Smith et al. 2008; Benjamin et al. 2016) model, to develop a polarimetric model of the ML and document statistical relationships in the ML to gain insight into the evolution of the microphysical processes above, within, and below the ML.

2. Methodology

The overarching goals of this study are 1) to create a large-scale database that documents polarimetric characteristics of the ML in stratiform rain events, and 2) to

use statistical relationships developed from that database to gain insight into the evolution of microphysical processes above, within, and below the ML. In total, the database included several hundred WSR-88D datasets collected during cold-season events. From that database, 33 WSR-88D datasets from 17 events were chosen for analysis in this study. Those datasets are listed in Table 1. To eliminate contributions from warm-season events, in which the microphysical structure of the ML might be influenced by nearby convection, particular care was taken to choose cold-season events that exhibited widespread regions of stratiform precipitation. As can be seen from Table 1, all events chosen for this analysis were collected during cold-season months (from late November through early March). Most also exhibited winter weather precipitation types (snow, wet snow, ice pellets, and freezing rain) within the radar domain. The events were manually inspected to ensure they exhibited distinct ML polarimetric signatures that were high enough above the surface to allow for calculation of variables at 0.3 km below the ML. The elevation angles of the cases were selected based on comparison of the ML QVP data at the 9.9°–19.5° angles for each case. The elevation angle with the most distinct ML signature (and with a ML that was high enough above the surface to allow for calculation of variables just below the ML) was selected for that event.

The events listed in Table 1 constitute approximately 400 h of data. In that sense, this study is probably most similar to that of Fabry and Zawadzki (1995, hereinafter FZ95), who used vertical profiles of reflectivity obtained from 600 h of vertically pointing X-band radar data (and 50 h of UHF boundary layer wind profiler data) to produce quantitative analysis of microphysical processes through the ML. While their results are valuable, they lack a polarimetric perspective that can reveal characteristics of the ML that reflectivity data alone are not able to provide. We now present the method for identifying the ML in the radar data and extracting polarimetric variables above, within, and below the ML of those events.

a. QVPs

As noted earlier, we utilize QVP methodology to study polarimetric signatures above, within, and below the ML of winter precipitation systems. As documented by Ryzhkov et al. (2016) and Griffin et al. (2018), QVPs can be constructed by azimuthally averaging Z_H , Z_{DR} , ρ_{hv} , and Φ_{DP} fields at relatively high antenna elevation angles of 10°–20°. Use of these high elevation angles reduces the effects of beam broadening and horizontal inhomogeneity, which allows for quantifying polarimetric characteristics of clouds and precipitation with high vertical resolution and dramatically improved statistical accuracy (Ryzhkov et al. 2016). The resulting

TABLE 1. QVP winter ML events, including their dates, radars, radar elevation angles, and periods for 17 ML winter precipitation events that were observed from the perspective of the 33 QVPs used in this study.

Date	Radar	Elev (°)	Time (UTC)
28 Jan 2014	KJGX	19.5	1314–0000
	KMOB	19.5	1218–0000
	KCLX	19.5	1910–2356
	KLCH	19.5	1109–2300
29 Jan 2014	KLTX	19.5	0004–1000
1 Feb 2014	KEAX	12.5	0353–1700
3 Feb 2014	KDIX	19.5	0641–1900
4 Feb 2014	KPAH	9.9	1553–0000
11 Feb 2014	KLTX	19.5	0900–0000
	KGWX	19.5	0006–0000
	KMHX	19.5	0352–2400
	KFFC	9.9	0008–1600
	KGSP	12.5	1438–0000
12 Feb 2014	KRAX	14.6	0809–0000
	KFFC	9.9	0212–0000
	KJGX	19.5	0244–0000
	KLTX	19.5	0614–2030
	KCLX	14.6	0009–2351
13 Feb 2014	KDGX	10.0	0006–1955
	KBMX	14.6	0119–2243
	KGSP	12.5	0004–1500
	KTLX	19.5	1801–2207
	KLVX	19.5	0321–2219
21 Feb 2015	KFFC	19.5	1400–0000
	KBMX	9.9	1224–2355
3 Mar 2015	KCLE	14.6	1156–0000
4 Mar 2015	KLVX	19.5	0326–0000
	KPAH	19.5	0026–0000
	KVWX	19.5	0007–0000
5 Mar 2015	KLWX	9.9	0009–2100
27 Nov 2015	KLTX	19.5	1006–2000
27 Dec 2015	KVNX	10.0	0004–1834
22 Jan 2016	KRAX	9.9	0546–0000

QVPs display the polarimetric variables in a convenient time-versus-height format, which allows for efficient investigation of key cloud microphysical processes and their temporal evolution. The QVP's higher vertical resolution and reduced noisiness in the polarimetric signatures allows for observation of smaller-scale features that would not be observable using range height indicators reconstructed from plan-position indicator scans with lower resolution. QVPs, including methods to extract δ and accurately compute K_{DP} in the ML, are discussed in more detail by both Ryzhkov et al. (2016) and Griffin et al. (2018).

In this study, QVPs are constructed using azimuthal medians of the polarimetric radar fields, rather than azimuthal averaging as in Ryzhkov et al. (2016) and Griffin et al. (2018). After comparing ML detection results, it was found that using medians rather than averages of the polarimetric radar data provides more realistic detection

of the ML, particularly in terms of ML depth and K_{DP} values. Specifically, results using azimuthal medians exhibit a shallower, more realistic, and tighter-looking ML signature with slightly smaller K_{DP} values (on the order of $0.01^\circ \text{ km}^{-1}$) when compared to the averaging results. The comparatively smaller K_{DP} values are more representative of the datasets since the majority of the QVP K_{DP} values in the 17 cases are small and are not “washed out” by averaging.

b. Defining the top and bottom of the ML

A crucial step in examining polarimetric and microphysical characteristics of the ML is to accurately define both the top and bottom of the ML. In their study, FZ95 capitalized on the fact that vertical profiles of Z_H through the ML (see their Fig. 1) are typically characterized by a sharp increase/decrease in reflectivity at the top/bottom (associated, respectively, with the heights where melting begins/ends) of the ML. By determining the heights of maximum curvature associated with these points, FZ95 were able to determine physically relevant heights associated with both the top and bottom of the ML. For the FZ95 method (hereinafter also referred to as the curvature method) to be successful, however, FZ95 noted that it was necessary for the vertical profile of reflectivity to exhibit strong curvature at both the top and bottom of the ML, and not elsewhere. In this study, we seek to develop a polarimetric method for determining the top and bottom of the ML that not only closely replicates the results of FZ95, but also provides heights for the ML top and bottom in regions of weak reflectivity where polarimetric signatures of a ML are strong but the FZ95 curvature method was found to frequently fail.

Since the onset of melting also results in an increase in hydrometeor diversity, the most logical polarimetric method to determine the height of the ML top and bottom is to utilize ρ_{hv} (Giangrande et al. 2008). For each event analyzed, the height of minimum ρ_{hv} was first determined for a narrow height interval that encompassed the ML and HRRR-model-estimated 0°C isotherm over the entire period of that event. Once the height of the minimum ρ_{hv} was found, an upward/downward search was conducted from that point to find the ML top/bottom heights associated with the first occurrence of ρ_{hv} that exceeded a predefined threshold. After testing this method on several events, a threshold of $\rho_{hv} \geq 0.97$ was found to exhibit the best agreement with the curvature results of FZ95. Overall, the heights of the ML top and ML bottom for the FZ95 curvature and polarimetric methods compare well within regions of higher Z_H , with the FZ95 curvature method exhibiting slightly higher (i.e., approximately 200 m) ML tops and slightly

higher or lower (i.e., approximately 50 m) ML bottoms. Within regions of $Z_H < 20 \text{ dBZ}$, the FZ95 method frequently failed.

c. Polarimetric signatures above, within, and below the ML

An example of the application of our method to a winter storm is illustrated by Fig. 1, which shows a time series of QVPs from the KFFC (Atlanta, Georgia) WSR-88D on 11 February 2014. Contours of HRRR model wet-bulb temperature ($^\circ\text{C}$) are overlaid in each plot, for interpretation of the radar data. As can be seen in Fig. 1, a well-defined ML is difficult to discern from approximately 0000 to 0300 UTC using Z_H alone (Fig. 1a), during which the curvature method of FZ95 failed to produce accurate results. On the other hand, a distinct ML signature is clearly evident in the Z_{DR} and ρ_{hv} fields (Figs. 1b,c) over this same period. Results from the polarimetric method of ML top/bottom height detection are depicted in Fig. 1 by the solid black lines overlaid on each polarimetric variable, showing good overall visual consistency with the ML as depicted by the Z_{DR} and ρ_{hv} fields. Note that all Z_{DR} measurements are corrected for hardware offset bias, according to the preprocessing procedures detailed by Ryzhkov et al. (2005). This ensures Z_{DR} in heavily aggregated snow is approximately 0.1–0.2 dB, and Z_{DR} in pure rain near the surface is 0–5 dB, for consistency across all cases in this investigation.

Once the ML top/bottom heights were determined, each time period was examined to derive 24 polarimetric characteristics above, within, and below the ML. These 24 polarimetric characteristics are listed and defined in Table 2 and are used throughout the remainder of the text to examine polarimetric and microphysical features in the vicinity of the ML. To examine microphysically driven connections between the ML and the DGL, the table also includes polarimetric variables derived from the DGL, as discussed by Griffin et al. (2018).

3. Data analysis

In this section, we present data from S-band polarimetric WSR-88D QVPs at high elevation angles (i.e., 9.9° – 19.5°) for the datasets presented in Table 1. The ML events occurred within stratiform precipitation over radars located in the southern, midwestern, and northeastern United States. Since the events presented in Table 1 constitute more than 400 h of observations and thousands of data points, composite histograms and composite density scatterplots are used to more effectively demonstrate the statistical relationships between the polarimetric variables. Weighted polynomial

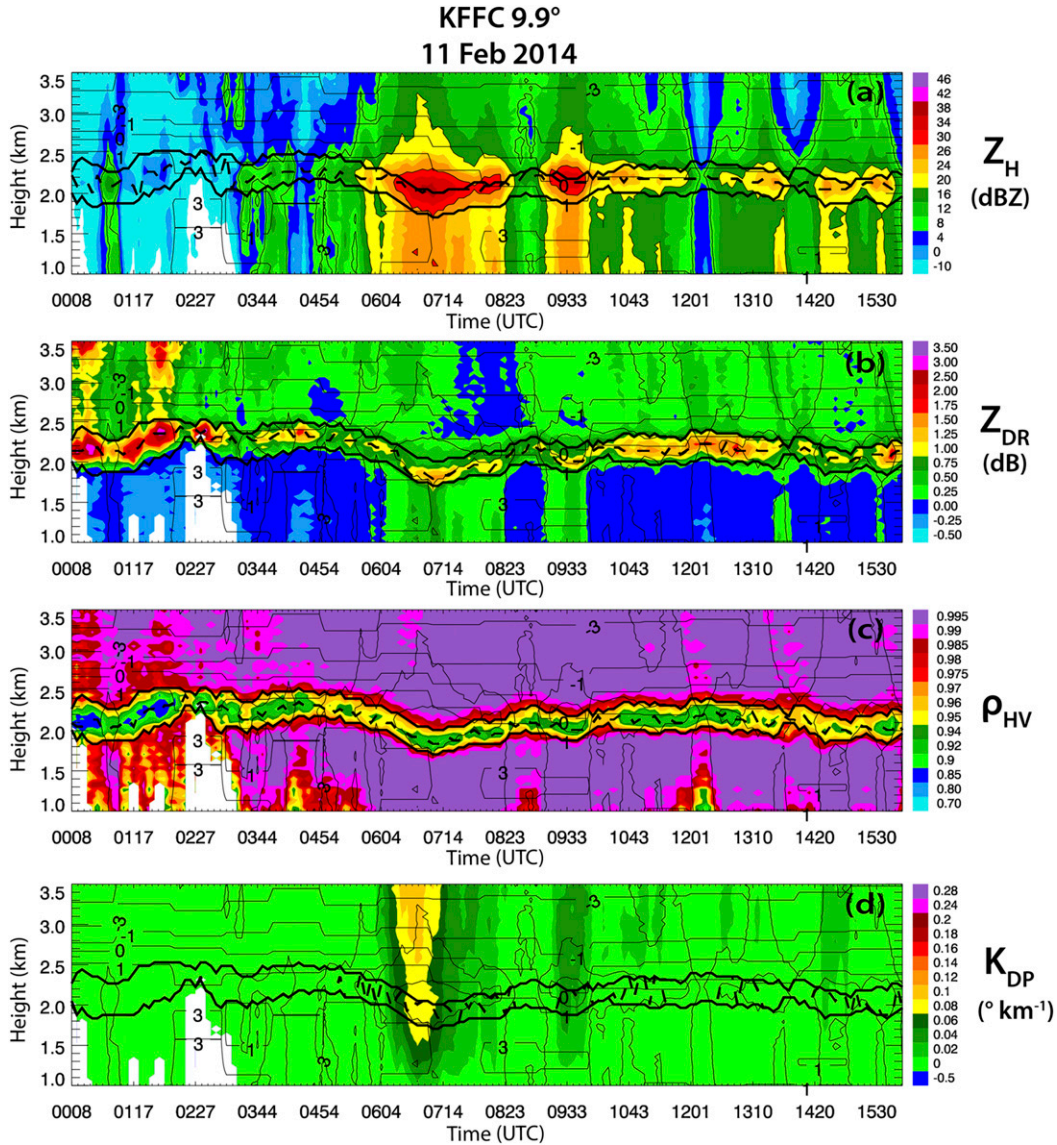


FIG. 1. QVPs of (a) Z_H (dBZ), (b) Z_{DR} (dB), (c) ρ_{hv} , and (d) K_{DP} ($^{\circ} \text{km}^{-1}$) for KFFC from 0008 through 1530 UTC 11 Feb 2014, at 9.9° elevation. Contours of HRRR model wet-bulb temperature ($^{\circ}\text{C}$) are overlaid in each plot. Also, Z_H is contoured at 10, 20, 30, and 40 dBZ. The ML top and bottom are represented by the thick black lines, and the thick dashed line between them represents the height of maximum Z_H , Z_{DR} , or K_{DP} or minimum ρ_{hv} .

regressions are also implemented to obtain the most accurate fits while reducing the influence of any significant outliers.

a. Polarimetric statistics of the ML

Figures 2a–f present composite (computed using ML data obtained from QVPs of all of the events listed in Table 1) histograms of maximum Z_H in the ML, maximum Z_{DR} in the ML, maximum K_{DP} in the ML, minimum ρ_{hv} in the ML, enhancement of Z_H (i.e., $\Delta Z = \text{maximum } Z_H \text{ in ML} - Z_H \text{ in rain}$), and maximum Φ_{DP} (i.e., δ) in the ML, respectively, while Fig. 3

represents a composite histogram of ML depth (ΔH). Note that the system differential phase is removed prior to computing the Φ_{DP} values presented in Fig. 2. Since the radar beam only passes through a few kilometers of precipitation prior to encountering the ML, the Φ_{DP} measurement within the ML typically provides an accurate representation of δ in the ML. Therefore, δ is hereinafter used to define maximum Φ_{DP} . Note that these values are significantly smaller than the one shown for an individual radial in Fig. 2 of Griffin et al. (2018). This is due to a Φ_{DP} processing error in Griffin et al. (2018) that resulted in some Φ_{DP} values not being unfolded

TABLE 2. Polarimetric variables derived from above, within, and below the ML. Variables derived from the DGL are also included (Griffin et al. 2018).

Variable	Definition
MLtopHeight	Height of ML top
MLbotHeight	Height of ML bottom
MLdepth	Depth of ML
ΔZ_H	Enhancement of Z_H (i.e., Max Z_H in ML – Z_H in rain)
MLmax Z_H	Max Z_H in ML
MLmax Z_{DR}	Max Z_{DR} in ML
MLmin ρ_{hv}	Min ρ_{hv} in ML
MLmax δ	Max Φ_{DP} (i.e., δ) in ML
MLmax K_{DP}	Max K_{DP} in ML
MLmax Z_H Height	Height of the max Z_H in the ML
MLmax Z_{DR} Height	Height of the max Z_{DR} in the ML
MLmin ρ_{hv} Height	Height of the min ρ_{hv} in the ML
MLmax δ Height	Height of the max δ in the ML
MLmax K_{DP} Height	Height of the max K_{DP} in the ML
Z_H Snow	Z_H at 0.3 km above MLtopHeight
Z_{DR} Snow	Z_{DR} at 0.3 km above MLtopHeight
ρ_{hv} Snow	ρ_{hv} at 0.3 km above MLtopHeight
δ Snow	δ at 0.3 km above MLtopHeight
K_{DP} Snow	K_{DP} at 0.3 km above MLtopHeight
Z_H Rain	Z_H at 0.3 km below MLbotHeight
Z_{DR} Rain	Z_{DR} at 0.3 km below MLbotHeight
ρ_{hv} Rain	ρ_{hv} at 0.3 km below MLbotHeight
δ Rain	δ at 0.3 km below MLbotHeight
K_{DP} Rain	K_{DP} at 0.3 km below MLbotHeight
DGLmax Z_H	90th-percentile max Z_H in DGL
DGLmax Z_{DR}	90th-percentile max Z_{DR} in DGL
DGLmin ρ_{hv}	90th-percentile min ρ_{hv} in DGL
DGLmax K_{DP}	90th-percentile max K_{DP} in DGL

correctly before computing QVP averages. With the revised methodology presented in this paper, which includes using median values, this error has been corrected, resulting in more accurate Φ_{DP} values. Each of the histograms also include overlays of corresponding distributions of ML data for which $Z_H < 20$ dBZ (indicated by the orange lines) and $Z_H \geq 20$ dBZ (indicated by the blue lines). These data are included since analyses using the FZ95 curvature ML detection method frequently failed for $Z_H < 20$ dBZ and the two ML Z_H regimes are apparent in trends in the data, analyzed later in the paper.

As will be discussed, these distributions exhibit both similarities and differences compared to X-band polarimetric ML distributions documented by Wolfensberger et al. (2015) and Trömel et al. (2017, 2019). It is important to note that the QVP-based histograms of polarimetric variables in the ML in Fig. 6 of Trömel et al. (2019) improve upon the RHI-based analyses in Fig. 15 of Wolfensberger et al. (2015). The distributions in Trömel et al. (2017, 2019) are narrower than those in Wolfensberger et al. (2015) due to the resolution

differences in QVP versus RHI methods. In general, implementation of the QVP method produces more narrow histograms and more accurate quantification of polarimetric variables compared to those using the RHI method.

In Fig. 2, the distribution of maximum Z_H in the ML ranges from -10 to 50 dBZ, with an overall average of 25 dBZ (Fig. 2a), and maximum Z_{DR} in the ML ranges between ~ 0 and 4 dB, with an average of 1.3 dB (Fig. 2b). Also, Fig. 2d illustrates corresponding minimum ρ_{hv} in the ML between 0.84 and 1.0 , with an overall average of 0.94 . Aside from the inclusion of data for $Z_H < 0$ dBZ, the shapes and mean values of the Z_H , Z_{DR} , and ρ_{hv} distributions closely agree with those documented at X band by Wolfensberger et al. (2015) and Trömel et al. (2017, 2019). A comparison of the results in Figs. 2a,b,d, Fig. 15 in Wolfensberger et al. (2015), and Fig. 6 in Trömel et al. (2019) shows that all three studies exhibit Z_H distributions that are noticeably skewed toward higher Z_H near 30 dBZ, the greatest Z_{DR} densities occurring between 0 and 2 dB, and ρ_{hv} distributions peaking near 0.95 .

In Fig. 2c, maximum K_{DP} in the ML ranges between 0° and $0.25^\circ \text{ km}^{-1}$, with an average of $0.02^\circ \text{ km}^{-1}$ both overall and within $Z \geq 20$ dBZ and a comparatively lower mean K_{DP} of $1.4 \times 10^{-40} \text{ km}^{-1}$ within low Z_H (likely resulting from a low concentration of pristine crystals). These are the first QVP K_{DP} measurements in MLs documented at S band. Note that the K_{DP} values within low Z_H in Fig. 2c are too small to view alongside the rest of the K_{DP} dataset. The K_{DP} distribution is noticeably weighted toward smaller values, with the majority of the dataset occurring between 0° and $0.1^\circ \text{ km}^{-1}$. After scaling and taking into account the difference in radar wavelength, these K_{DP} values are comparable to those documented by Wolfensberger et al. (2015) and Trömel et al. (2019). The shape of the distribution is similar to that of Trömel et al. (2019), who observed composite mean K_{DP} in the ML of $0.19^\circ \text{ km}^{-1}$ with values ranging between approximately 0.06° and $0.33^\circ \text{ km}^{-1}$ at X band, while Wolfensberger et al. (2015) observed composite mean K_{DP} in the ML of $0.11^\circ \text{ km}^{-1}$ with values ranging between approximately -0.5° and $1.5^\circ \text{ km}^{-1}$ at X band.

In Fig. 2e, the enhancement of Z_H (i.e., $\Delta Z =$ maximum Z_H in ML – Z_H in rain) varies between approximately -5 and 15 dBZ, with an overall mean of 5.8 dBZ. This suggests that Z_H in the ML is on average 5.8 dBZ greater than that of Z_H in rain, which can be valuable information for improving rainfall estimation in brightband regions. Next, in Fig. 2f, δ in the ML generally ranges between 0° and 5° and reaches up to 10° with an overall mean of 1.63° . The δ within $Z_H < 20$ dBZ in the ML ranges between approximately -7 and 3° , with a smaller mean

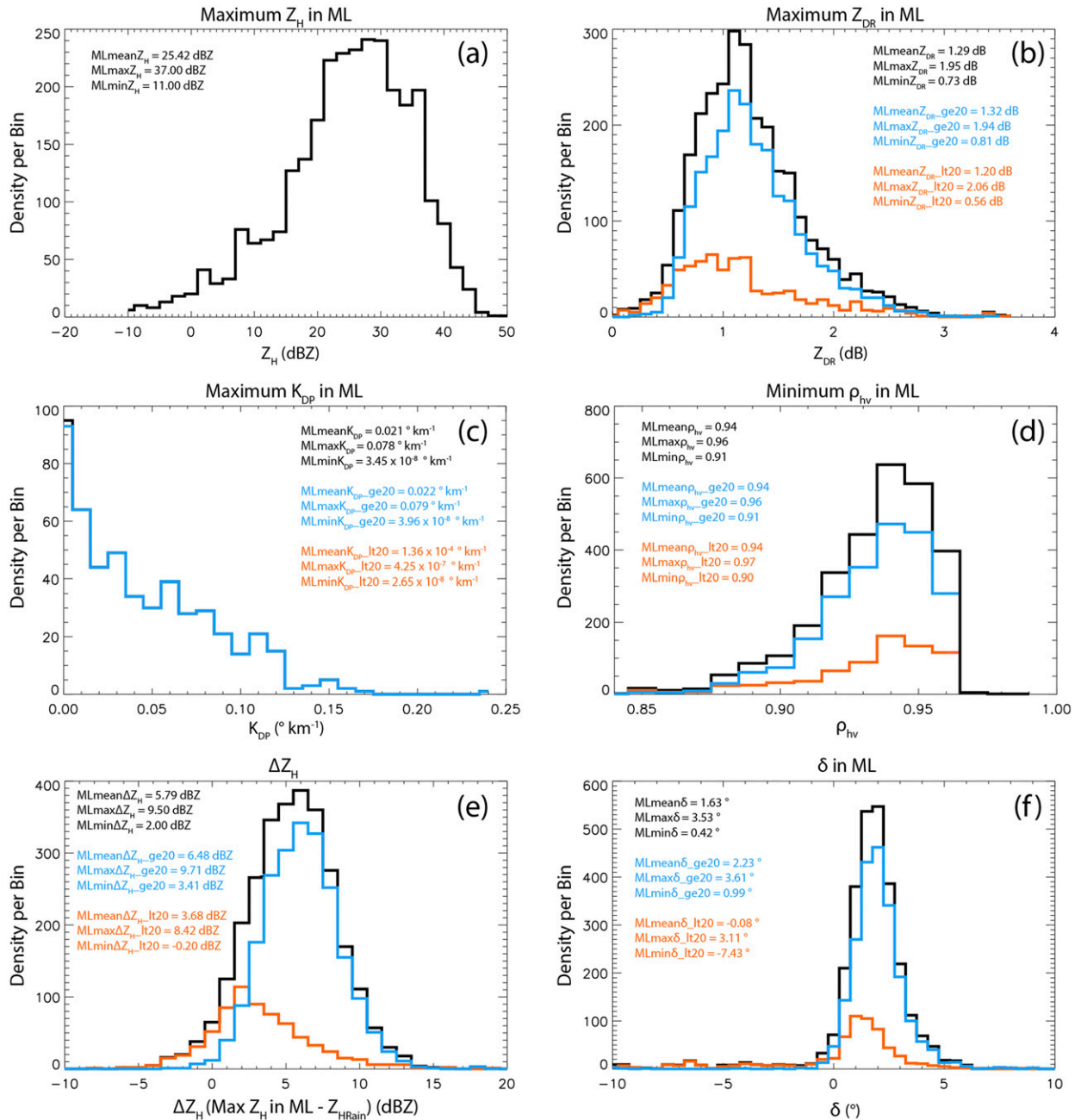


FIG. 2. Composite histograms of (a) maximum Z_H in the ML (dBZ), (b) maximum Z_{DR} in the ML (dB), (c) maximum K_{DP} in the ML (° km⁻¹), (d) minimum ρ_{hv} in the ML, (e) ΔZ_H (i.e., Z_H in ML - Z_H in rain; dBZ), and (f) δ (°) in the ML, for the 33 QVP ML events. Mean, 90th-percentile maximum (indicated as max), and 10th-percentile minimum (indicated as min) values of the variables are indicated in each panel, for the total dataset (represented by the thick black lines), the data corresponding to $Z_H < 20$ dBZ (represented by the orange lines), and the data corresponding to $Z_H \geq 20$ dBZ (represented by the blue lines).

of -0.08° (orange line in Fig. 2f) as compared with that of 2.23° for δ within $Z_H \geq 20$ dBZ (blue line in Fig. 2f). Wolfensberger et al. (2015) do not include δ analyses, but Trömel et al. (2017, 2019) document δ in the ML at X band, with a mean of 1.8° and maximum values up to 5° , which are slightly smaller than but comparable to

those observed in the present study. Also, the shape of the total δ distribution compares well for values between 0° and 5° , where peak densities occur in both distributions (Figs. 2f and 6 in Trömel et al. 2019). The total δ distribution is skewed toward lower values (i.e., from approximately -1° to 3°) within low Z_H regions in

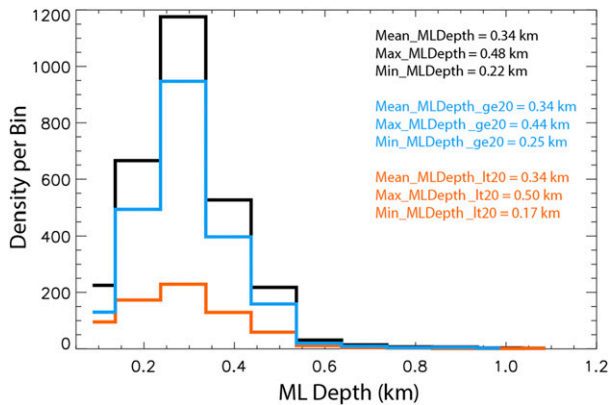


FIG. 3. As in Fig. 2, but for ML depth (km).

the ML and toward slightly higher values (i.e., mostly between 0° and 5°) within regions of larger Z_H in the ML. According to Trömel et al. (2017, 2019), although positive values of δ are most common, negative δ can also occur; the estimates of δ are obtained by integrating over the full particle size spectrum. They suggest that, at X band, large negative δ associated with melting particles in the middle of the ML may cancel out positive δ associated with other hydrometeors, resulting in smaller magnitudes of δ compared with those at S band. They further explain that larger δ magnitudes can likely result from the occurrence of large, partially melted snowflakes that increase in size via riming and aggregation.

The composite histogram of ML depth in Fig. 3 reveals an average ML depth of 340 m, with depths as small as approximately 100 m and as large as approximately 1100 m. The shape and magnitude of the distribution are similar to those of Wolfensberger et al. (2015) and Giangrande et al. (2008). Giangrande et al. (2008) observed typical ML thicknesses of approximately

300 m with a long right tail and Wolfensberger et al. (2015) document ML thicknesses ranging between 175 and 600 m, with an average of 320 m. Trömel et al. (2019) also observed ML thicknesses between approximately 100 and 500 m in Bonn, Germany. Other similar statistical observations of ML depth are documented by Bandera et al. (1998) and Durden et al. (1997). For data within $Z \geq 20$ dBZ, the minimum ML depth of 100 m and maximum ML depth of 1000 m (e.g., Fig. 3; blue line) closely compares with that observed by FZ95, who document brightband thicknesses ranging between approximately 150 and 900 m (e.g., Fig. 6 in FZ95), which is expected since our polarimetric ML detection method was developed to closely approximate the results of FZ95 curvature method.

b. Scatterplot comparisons of polarimetric relationships

1) δ IN THE ML

A notable feature of the polarimetric QVP ML data is the values of δ observed at S band. As depicted in each of the composite scatterplots in Figs. 4a and 4b, the largest δ in the ML reaches approximately 8° , while the majority of the δ values observed in the dataset fell between 0° and 4° , which is significantly smaller than the S-band observations of δ up to 70° reported by Trömel et al. (2014). It is very likely that very high values of δ at S band reported in the Trömel et al. (2014) study were the result of a processing error of Φ_{DP} . Note that non-density composite scatterplots are used here to focus on the extent of the δ values. In Fig. 4a, the relationship between maximum δ and maximum Z_H in the ML is depicted. Although the majority of the $\delta > 4^\circ$ values occur for $Z_H \geq 20$ dBZ, there are also a significant number of $\delta > 4^\circ$ data points within very low $Z_H < 20$ dBZ in the

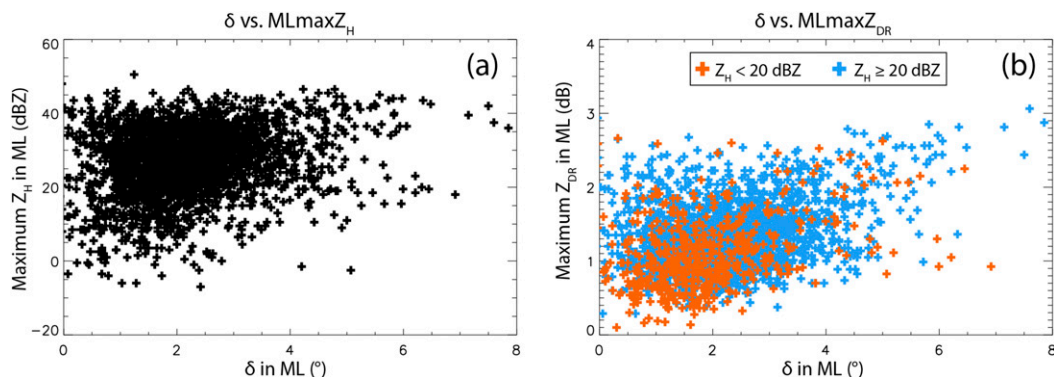


FIG. 4. Composite scatterplots of (a) δ in the ML ($^\circ$) vs maximum Z_H in the ML (dBZ) and (b) δ in the ML vs maximum Z_{DR} in the ML (dB), for the 33 QVP ML events. Orange and blue data points represent ML data for which $Z_H < 20$ dBZ and $Z_H \geq 20$ dBZ, respectively.

ML (Fig. 4a). Figure 4b also illustrates that δ is correlated with Z_{DR} in the ML. For example, in Fig. 4b, positive correlation is evident between maximum δ and maximum Z_{DR} in the ML, with the larger δ generally occurring for larger Z_{DR} . Specifically, Z_{DR} ranges between 0 and 4 dB within δ ranging up to 8° . The orange and blue data points represent ML data for which $Z_H < 20$ dBZ and $Z_H \geq 20$ dBZ, respectively. These results support those of Trömel et al. (2013, 2017, 2019), who observed strong interdependence between maximum Z_{DR} and δ in the ML at X band. It is expected that excluding the outlying cluster of data for which $\delta > 4^\circ$ would result in stronger correlations in Fig. 4b. Overall, the larger Z_{DR} in the ML generally occur with larger δ (Fig. 4b), potentially indicating more efficient aggregation above the ML (Fridlind et al. 2017; Trömel et al. 2014; Ryzhkov et al. 2016) and larger-sized partially melted snowflakes in the ML (Trömel et al. 2013, 2014), as the ice particles acquire more liquid meltwater and become more oblate as they fall through the ML.

The estimated maximal values of δ in this study are closer to the ones reported by Zrnić et al. (1993; 10° – 15°) and mentioned by Melnikov et al. (2005; 10°). Zrnić et al. (1993) observed δ up to 10° – 15° for large (>10 mm), oblate, and spongy (water soaked) aggregates and explain that a significant increase in δ can occur when hydrometeors are large enough to scatter in the resonant regime. They also explain that if an aggregate is coated with a sufficient amount of water (i.e., if thickness of the water coating is 10% of the particle's radius), the resultant polarimetric radar signature is similar to that of an aggregate of the same size that is filled with water (i.e., a liquid hydrometeor; Zrnić et al. 1993). Melnikov et al. (2005) and Melnikov (2012) offered an explanation for mechanisms that might be responsible for δ enhancements in the ML, indicating that while δ is small for dry ice particles with any oblateness, it would be expected to see increases in δ for oblate wet particles that contain ice cores as oblateness increases and as a thick water coating forms on the particle. They also observed $\delta > 10^\circ$ for large and oblate spongy snowflakes. Furthermore, enhancement of δ in the ML as seen in Fig. 4 may suggest a reduction in tumbling snow aggregates. The width σ of the canting angle distribution within the DGL is approximately 10° (Matrosov et al. 2005; Melnikov and Straka 2013; Bukovčić et al. 2018), with dry aggregates more chaotically oriented below. As aggregation begins to dominate, σ increases to up to 40° (Hendry et al. 1987) and snowflakes become more randomly oriented (Bukovčić et al. 2018). Once aggregates begin to melt, they become more ordered and σ gradually reduces from approximately 40° in snow to less than 10° below the ML.

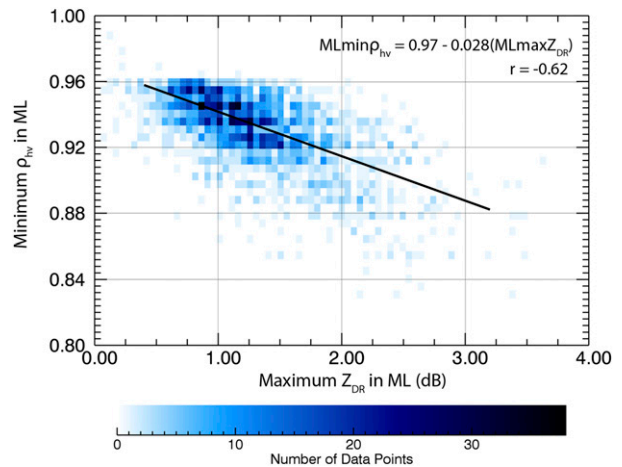


FIG. 5. Composite density scatterplot of maximum Z_{DR} in the ML (dB) vs minimum ρ_{hv} in the ML for the 33 QVP ML events. Negative correlation ($r = -0.62$) occurs between these variables as ice particles begin to melt as they fall through the ML and become more oblate as they become water coated.

2) MAXIMUM Z_{DR} VERSUS MINIMUM ρ_{HV} IN THE ML

Figure 5 presents a composite density scatterplot of maximum Z_{DR} in the ML versus minimum ρ_{hv} in the ML. Maximum Z_{DR} ranges mostly from 0 to 3 dB, with corresponding minimum ρ_{hv} between approximately 0.84 and 0.98. The majority of the dataset is represented by ρ_{hv} between approximately 0.88 and 0.96 and Z_{DR} between 0.5 and 2 dB, as is evidenced by the deeper blue colors representing the largest densities of data points. As expected, a negative correlation (i.e., $r = -0.62$) exists between the variables. As ice particles begin to melt as they fall through the ML, their dielectric constant and density increase and the larger partially melted snowflakes result in increased Z_{DR} and reduced ρ_{hv} in the ML. Correlation coefficient ρ_{hv} in the ML decreases with increasing liquid water, which further enhances diversity in hydrometeor types with different shapes and orientations (Illingworth and Caylor 1989; Balakrishnan and Zrnić 1990; Zrnić et al. 1993), since ρ_{hv} is a measure of variability of hydrometeors' shape, size, orientation, and phase composition.

3) TWO ML REGIMES

Another significant and repetitive feature of the 33 QVP ML events is the occurrence of two ML regimes: low Z_H (<20 dBZ) and higher Z_H (≥ 20 dBZ). As previously demonstrated in the KFFC 11 February 2014 9.9° QVP in Fig. 1, a region of higher Z_H distinctly indicates the presence and location of a ML, collocated with enhanced Z_{DR} and reduced ρ_{hv} in a layer between approximately 2 and 2.5 km during approximately 0500–1600 UTC

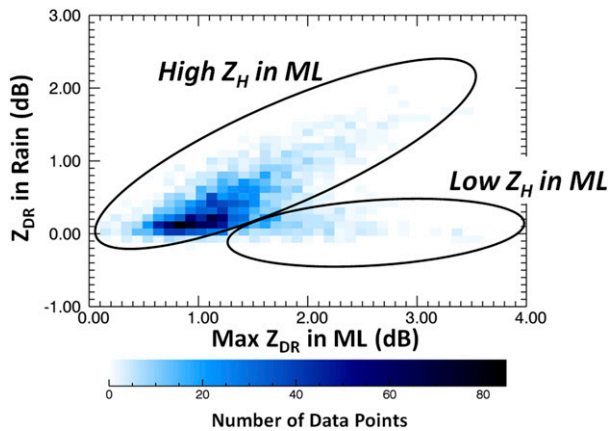


FIG. 6. Composite density scatterplot of maximum Z_{DR} in the ML vs Z_{DR} in rain for the 33 QVP ML events. Two ML regimes are evident: 1) lower Z_{DR} corresponding to higher Z_H in the ML, resulting in a distinct ML, and 2) higher Z_{DR} corresponding to low Z_H in the ML ($< \sim 20$ dBZ) where the ML is only identifiable in polarimetric imagery. In the second region, there is a small concentration of small hydrometeors including crystals such as dendrites and plates, resulting in higher Z_{DR} .

(Figs. 1a–c). On the other hand, prior to about 0300 UTC, a well-defined ML is difficult to discern from approximately 0000 to 0300 UTC using Z_H alone. During this period of weak Z_H (< 20 dBZ), the ML is only identifiable in the polarimetric imagery where a distinct ML signature is clearly evident in the Z_{DR} and ρ_{hv} fields (e.g., Figs. 1b,c, respectively). Here, the reduced Z_H and ρ_{hv} combined with enhanced Z_{DR} indicate a very low concentration of small hydrometeors including pristine crystals such as dendrites (0.01–1-mm maximum dimensions; Straka et al. 2000), plates (0.01–3-mm maximum dimensions; Straka et al. 2000), or needles that contribute to the enhanced Z_{DR} and reduced ρ_{hv} because of their very nonspherical shape within and above the ML. The low concentration of these small crystals and a lack of larger aggregates suggest an absence of aggregation, while the smaller particle sizes and their resultant quick melting produce a very shallow ML. Under such a scenario, the enhancement of Z_H in a thin ML is either similar to or lower than the one in the “mature” and thick ML where continuing aggregation of wet snowflakes within the bright band further increases the Z_H maximum. Beam smearing makes the very thin ML undetectable in terms of Z_H (even at close distances from the radar). However, such beam smearing may not dissolve the Z_{DR} and ρ_{hv} ML signatures because Z_{DR} is anomalously high and ρ_{hv} is very low for melting ice particles with very anisotropic shape. This fact emphasizes the benefit of polarimetric radar measurements for detecting extra thin MLs.

The two ML regimes are also evident in the composite density scatterplot in Fig. 6, which displays the relationship

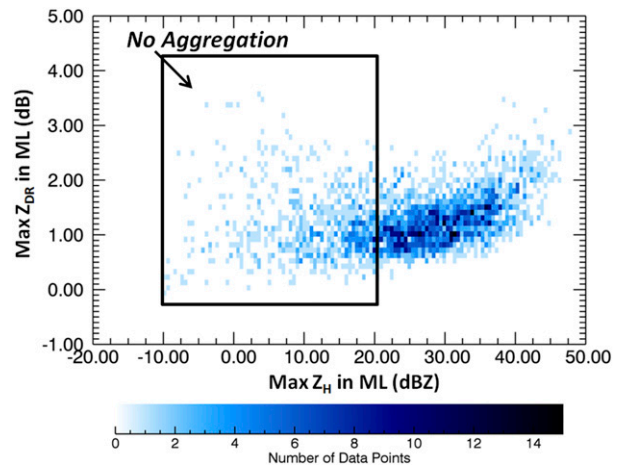


FIG. 7. Composite density scatterplot of maximum Z_H in the ML (dBZ) vs maximum Z_{DR} in the ML (dB) for the 33 QVP ML events. Low Z_H in the ML ($< \sim 20$ dBZ) occurs during larger Z_{DR} in the ML (~ 0 –4 dB) when pristine, nonaggregated ice falls through it. The increase in Z_H in the ML during the increase in maximum Z_{DR} in the ML indicates that the oblateness of particles increases as they become water coated through melting.

between maximum Z_{DR} in the ML and Z_{DR} in rain (i.e., 300 m below the bottom of the ML). The data show two distinct branches of high Z_{DR} in the ML, one related to high Z_H in the ML at times when aggregation is significant and the other related to low Z_H in the ML at times when nonaggregated pristine ice crystals are more prevalent (Fig. 6). If the data for low $Z_H < 20$ dBZ are filtered out, a strong relationship between maximum Z_{DR} in the ML and Z_{DR} in rain is evident (not shown), with higher Z_{DR} in the ML occurring with higher Z_{DR} in rain. This strong relationship is potentially valuable for improving future rainfall estimation in brightband regions, particularly at more distant ranges from the radar. Further evidence of the two ML regimes is provided in Fig. 7, which illustrates the nonmonotonic dependence of Z_{DR} on Z_H in the ML. When maximum Z_H in the ML ranges between approximately -10 and 20 dBZ, a broader range of Z_{DR} from 0 to 4 dB occurs as pristine, nonaggregated crystals fall through the ML. During larger maximum Z_H in the ML (i.e., ≥ 20 dBZ), a stronger relationship is apparent as larger Z_H generally coincides with increasing Z_{DR} in the ML. Overall, there is ample evidence that polarimetric radar data are much more valuable for detecting ML microphysical processes than conventional reflectivity data alone, particularly in regions of low Z_H .

4) K_{DP} MEASUREMENTS IN THE ML

Another feature of this investigation is the estimation of K_{DP} in the ML, documented for the first time at S band. Statistics of K_{DP} in the ML are important because

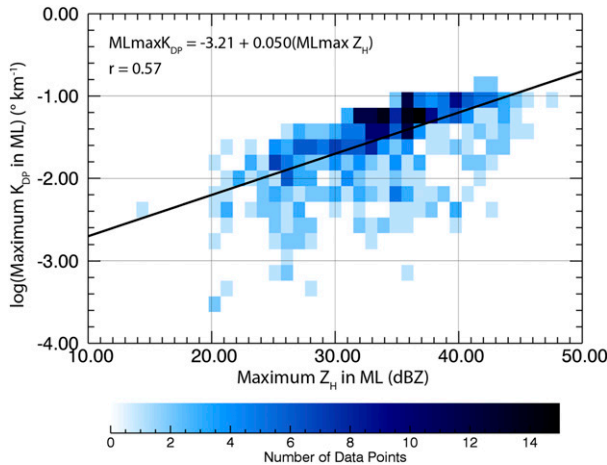


FIG. 8. Composite density scatterplot featuring a positive correlation ($r = 0.57$) between maximum Z_H in the ML (dBZ) and $\log(\text{maximum } K_{DP} \text{ in the ML})$ ($^{\circ} \text{ km}^{-1}$) for the 33 QVP ML events (at S band).

K_{DP} is expected to be better correlated with precipitation flux than Z_H and Z_{DR} , which are weighted by large wet aggregates, while K_{DP} is more weighted by small melting snowflakes and resulting raindrops and may be directly utilized for rainfall estimation in regions of brightband contamination (Borowska et al. 2011; Trömel et al. 2017, 2019). Figure 8 presents a composite density scatterplot demonstrating a positive correlation (i.e., 0.57) between maximum K_{DP} (up to $0.22^{\circ} \text{ km}^{-1}$) and maximum Z_H (from -10 to 50 dBZ) in the ML, with the greatest concentration of data occurring for K_{DP} ranging between approximately 0.001 and $0.22^{\circ} \text{ km}^{-1}$ within larger $Z_H > 20$ dBZ. This relationship provides confidence in the QVP processing routine implemented for K_{DP} estimation in the ML. Trömel et al. (2019) also observed a moderate relationship between K_{DP} and Z_H in the ML for the first time at X band, with a correlation of 0.51. Therefore, it is evident that K_{DP} measurements in the ML can be confidently used to examine ML microphysical processes and in turn optimize future microphysical models.

5) ML STATISTICS VALUABLE FOR PVPR AND QPE

The idea of a PVPR method implies parameterization of the intrinsic vertical profiles of radar reflectivity within the ML using polarimetric variables such as ρ_{hv} or Z_{DR} (Trömel et al. 2017, 2019; Ryzhkov and Znić 2019, their chapter 10). This includes analysis of statistical correlations between different variables of the vertical profile of Z_H and minimal value of ρ_{hv} , or maximal value of Z_{DR} within the ML. Figures 9 and 10 reveal statistics that are valuable for developing a PVPR technique that

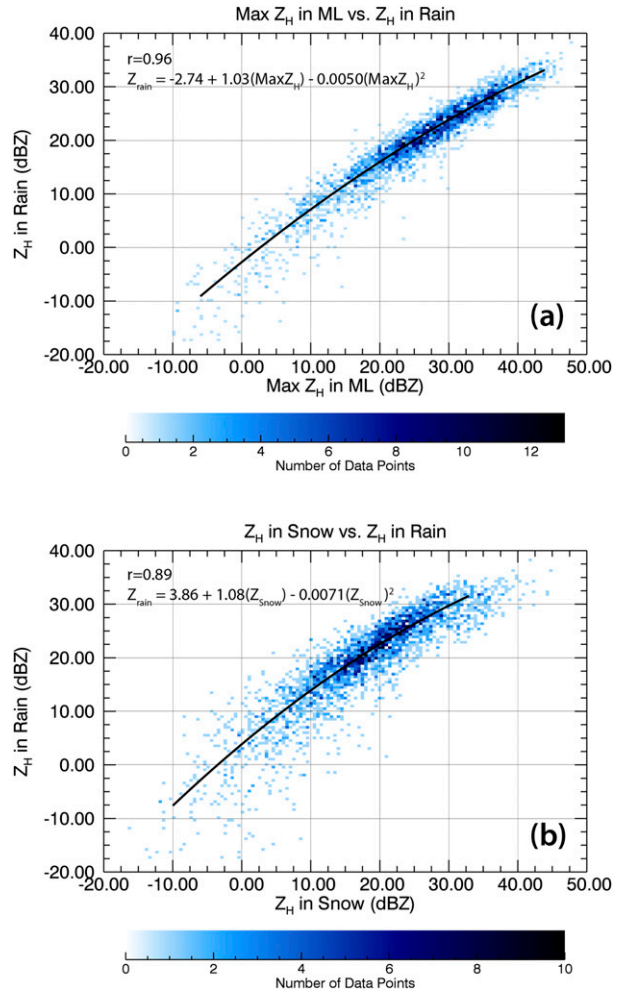


FIG. 9. Composite density scatterplots of (a) maximum Z_H in the ML vs Z_H in rain (dBZ) and (b) maximum Z_H in snow vs Z_H in rain (dBZ), for the 33 QVP ML events. Correlations between the variables are indicated in each panel. Note: Z_H in rain = Z_H at 0.3 km below ML bottom and Z_H in snow = Z_H at 0.3 km above ML top.

can help improve representation of ML microphysics in NWP models and also improve polarimetric QPE in rain. In Fig. 9a, correlation (i.e., 0.96) between maximum Z_H in the ML and Z_H in rain (i.e., 0.3 km below the bottom of the ML) is presented, with larger maximum Z_H in the ML from -10 to 50 dBZ occurring with larger Z_H in rain up to 40 dBZ. The majority of the data points occur for maximum Z_H in the ML between 10 and 40 dBZ and Z_H in rain between 10 and 30 dBZ. Trömel et al. (2019) also observed strong correlation (i.e., 0.93) between these variables at X band (e.g., Fig. 7 in Trömel et al. 2019). The correlation between these variables suggests that Z_H measurements in the ML can be used to estimate precipitation intensity near the surface in winter weather systems, where the height of the ML is typically very low. Furthermore, in Fig. 9b, correlation

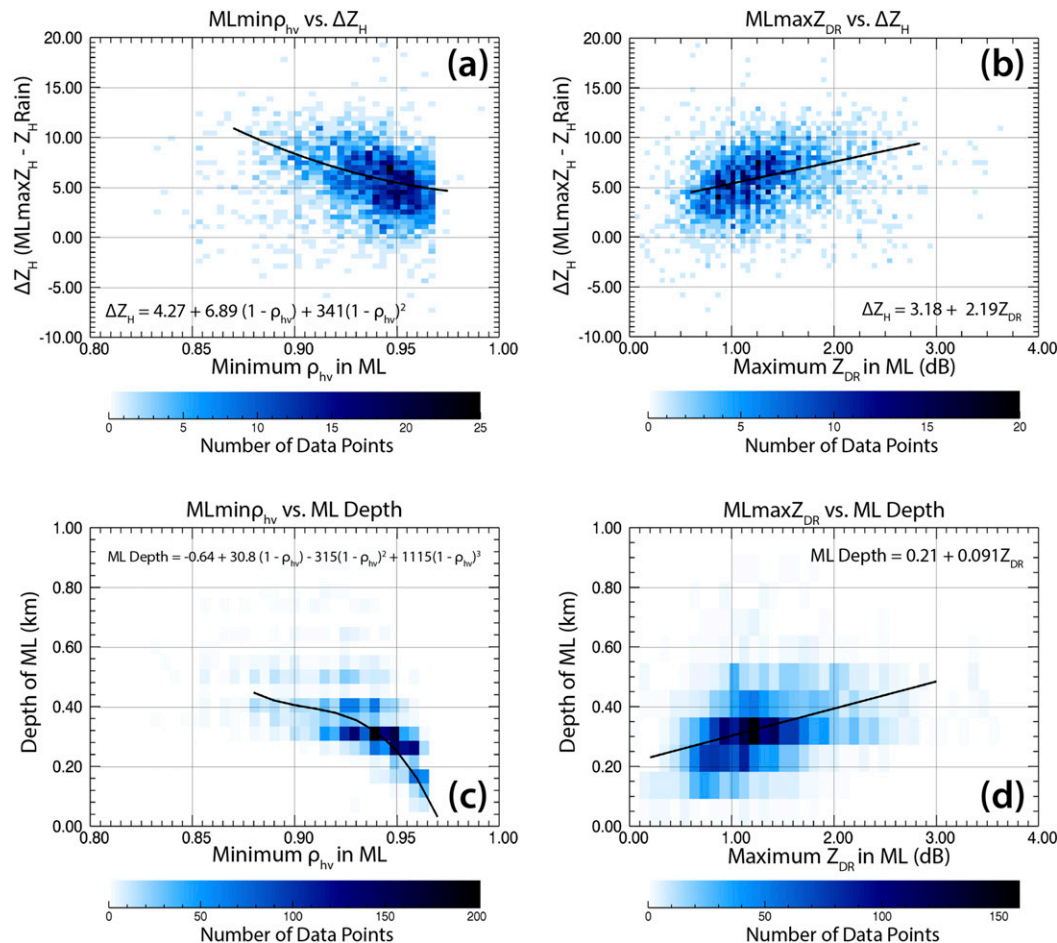


FIG. 10. Composite density scatterplots of (a) minimum ρ_{hv} in the ML vs ΔZ_H (dBZ), (b) maximum Z_{DR} in the ML (dB) vs ΔZ_H , (c) minimum ρ_{hv} in the ML vs ML depth (km), and (d) maximum Z_{DR} in the ML vs ML depth, for the 33 QVP ML events. Note: ΔZ_H = maximum Z_H in the ML - Z_H in rain.

(i.e., 0.89) exists between Z_H in snow (i.e., 0.3 km above the ML top) and Z_H in rain, with larger values of Z_H above the ML occurring during larger Z_H below the ML. Also, the greatest densities of data points occur between approximately 10 and 30 dBZ. These results suggest that larger values of Z_H above the ML can indicate greater Z_H in rain. Essentially, a higher concentration of snowflakes just above the ML can lead to more snowflakes falling into the ML and thus a higher concentration of raindrops falling below. Also, larger snowflakes above the ML can melt into larger raindrops below.

Figure 10 illustrates statistical correlations of the ML that are particularly important for developing a PVPR technique to mitigate the impact of ML contamination on QPE. Figure 10a reveals that negative correlation occurs between minimum ρ_{hv} in the ML and the corresponding enhancement of Z_H (i.e., $\Delta Z_H = Z_{Hmax} - Z_{Hrain}$). Greater differences between Z_{Hmax} in the ML and Z_{Hrain} are generally associated with lower minimum ρ_{hv} in the ML,

which bolsters the results of Trömel et al. (2017, 2019) at X band. Also, in Fig. 10b, a positive correlation exists between maximum Z_{DR} in the ML and ΔZ_H , with greater Z_{DR} in the ML generally occurring alongside greater ΔZ_H . The depth of the ML (i.e., difference between height of ML top and height of ML bottom) is correlated with minimum ρ_{hv} in the ML, with greater ML depths generally occurring during lower minimum ρ_{hv} in the ML (Fig. 10c). Note that the fit equation in Fig. 10c may not be applicable beyond the range of ρ_{hv} estimated in this particular study. Figure 10d illustrates correlation between ML depth and maximum Z_{DR} in the ML, with larger Z_{DR} in the ML generally occurring during larger ML depths. This is expected since larger particles take longer to melt and contribute to a deeper ML. Figure 11 displays the relationship between maximum Z_H in the ML and ML depth, with slightly larger ML depths generally occurring during larger Z_H in the ML. This correlation is at variance

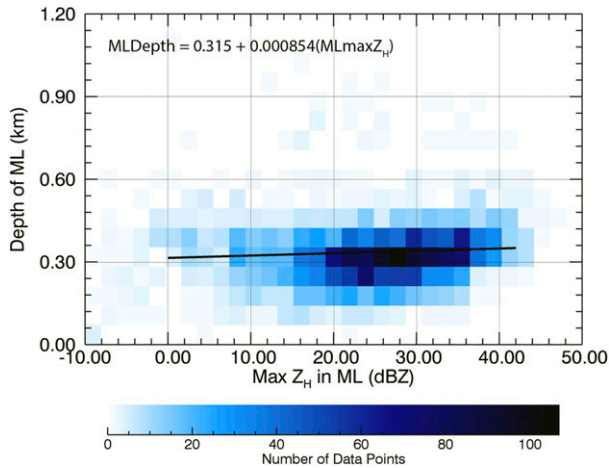


FIG. 11. Composite density scatterplot of maximum Z_H in the ML vs ML depth (km) for the 33 QVP ML events.

with the findings of Wolfensberger et al. (2015) in Switzerland who reported higher correlation between the two variables of the ML. The difference in correlation could potentially be due to difference in climate. Differences in resolution of the QVP versus RHI methods may also play a role. The greatest concentration of data occurs for ML depths between approximately 150 and 450 m during Z_H in the ML between 0 and 40 dBZ. Overall, these polarimetric statistics in the ML provide important information on microphysical properties within and near the ML and how they relate to the behavior of precipitation in rain, which can ultimately help improve the accuracy of polarimetric QPE in rain.

4. Discussion

The QVP polarimetric statistics presented in section 3 are valuable for advancing understanding of the relation of polarimetric signatures in the ML to the underlying physical processes of precipitation formation and evolution throughout the depth of a cloud. Our study that utilizes S-band radar measurements complements a similar investigation performed by Trömel et al. (2017, 2019) in Germany at X band. In general, the results are consistent and any differences between the two can be attributed to the differences in radar wavelengths and climate conditions between the United States and Europe.

Polarimetric properties of the ML are determined by the type of snow falling through it that has microphysical attributes most clearly manifested by the polarimetric signatures within the DGL in the temperature interval between -10° and -20°C (Griffin et al. 2018). Therefore, one should expect certain correlation between polarimetric signatures in the ML and DGL and, indeed, such

connections have been observed. For example, enhanced K_{DP} in the ML (up to 0.22°km^{-1}) was frequently found to be associated with enhanced K_{DP} in the DGL during 1) taller and colder cloud tops, 2) enhanced Z_{DR} and reduced ρ_{hv} in the ML (relative to adjacent times), and 3) sagging of the ML toward the surface (e.g., during $\sim 0600\text{--}0730$ UTC in Fig. 1 and during $\sim 0200\text{--}0400$ UTC in Fig. 12). Also, the enhanced K_{DP} in the DGL would sometimes extend down to the ML, indicating enhanced concentration of nonspherical ice particles above the ML (e.g., $\sim 0600\text{--}0730$ UTC in Fig. 1). Figure 13 illustrates the positive correlation (i.e., $r = 0.42$) observed between maximum K_{DP} in the DGL and maximum K_{DP} in the ML for all events listed in Table 1. Note that the fit equation in Fig. 13 may not be applicable beyond the range of K_{DP} estimated in this particular study. Enhanced K_{DP} in the ML is also found to occur during enhanced Z_H in the ML, which is illustrated by the linear correlation found between K_{DP} and Z_H in the ML (Fig. 8). Griffin et al. (2018) found that enhanced K_{DP} within the DGL are associated with taller and colder cloud tops. Higher K_{DP} within the DGL means higher ice water content (IWC) and precipitation flux (Ryzhkov et al. 2018), which increase the strength and depth of the ML once ice particles fall through it. These observations are consistent with the recent findings of Carlin and Ryzhkov (2019), who used a one-dimensional spectral bin model of melting snow (i.e., 1D-MS) to investigate the relation between polarimetric characteristics of modeled MLs and the maximum diabatic cooling rates within them. They discovered that K_{DP} is strongly correlated with diabatic cooling rate due to melting of particles in the ML, which can lead to a dip in the height of the ML bottom often termed as “sagging” of the ML. This suggests that accurate K_{DP} measurements can be used to retrieve maximum cooling rate within the ML. Carlin and Ryzhkov (2019) also discuss other microphysical processes that could cause sagging brightband signatures, including riming, aggregation, and increased precipitation intensity and the cooling that ensues. In another study, Kumjian et al. (2016) investigate dips in MLs and document that denser, more isometric ice falling into the ML can cause sagging of bright bands, which is significant since rimed particles above the ML can indicate supercooled liquid water that can cause hazardous aircraft icing. In general, the ability to use QVPs to estimate K_{DP} in the ML for the first time (e.g., Trömel et al. 2017, 2019; Griffin et al. 2018) combined with the understanding of how K_{DP} can be used to estimate ML cooling rates allows for potential improvement to Z_H -based ML cooling rate estimation methods (e.g., Carlin and Ryzhkov 2019) and a better understanding of the causes of brightband sagging.

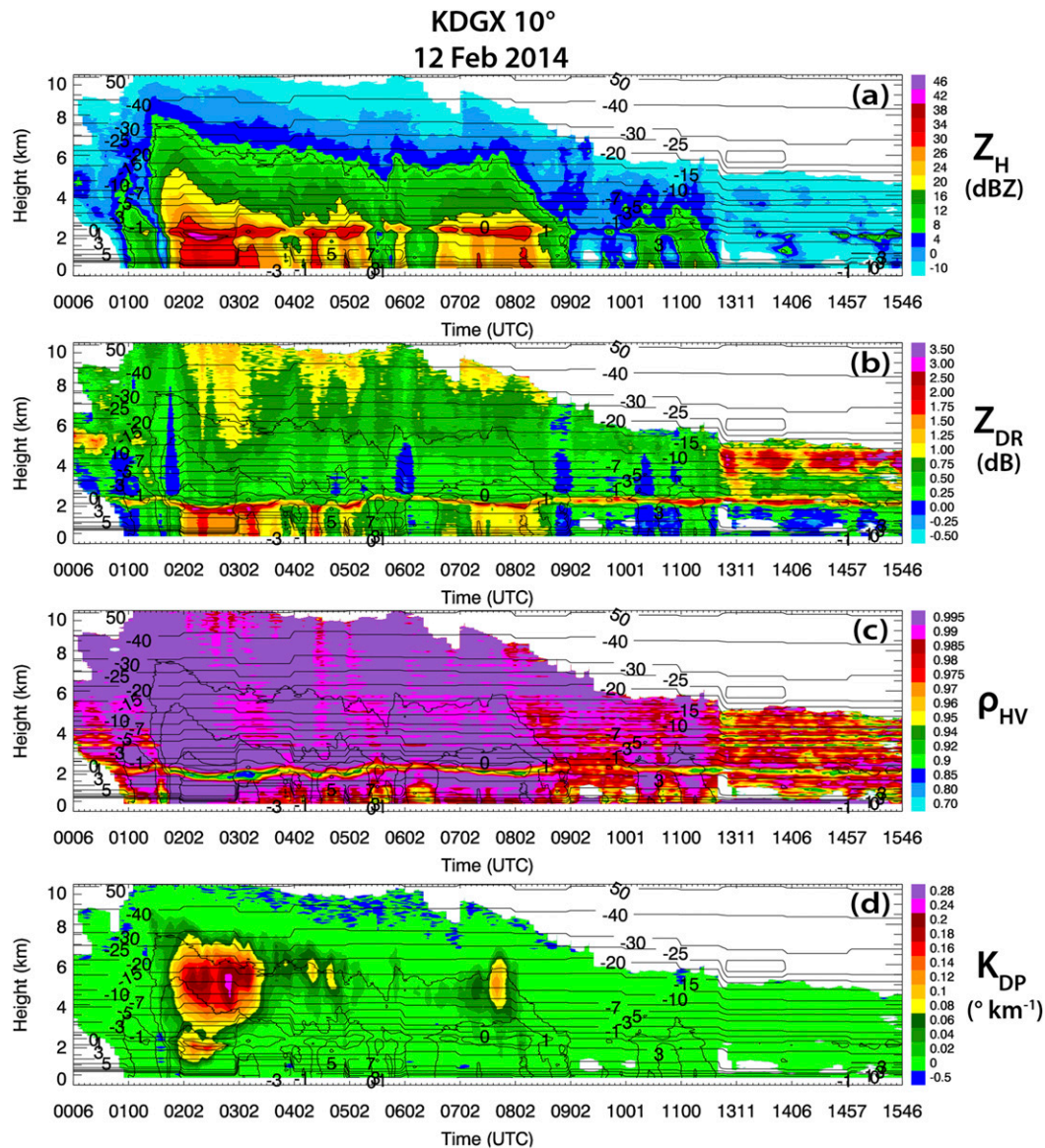


FIG. 12. QVPs of (a) Z_H (dBZ), (b) Z_{DR} (dB), (c) ρ_{HV} , and (d) K_{DP} ($^{\circ} \text{km}^{-1}$) for KDGX from 0006 through 1500 UTC 12 Feb 2014, at 10° elevation. Contours of HRRR model wet-bulb temperature ($^{\circ}\text{C}$) are overlaid in each plot. Also, Z_H is contoured at 10, 20, 30, and 40 dBZ.

Quantification of polarimetric variables in and above the ML not only provides details of the complexity of ML microphysics and what they reveal about ice processes above, but it can also be used to relate elevated microphysical processes to precipitation characteristics near the surface, helping to better inform numerical weather prediction models.

5. Summary

This study uses quasi-vertical profiles obtained from a large-scale database of U.S. WSR-88D S-band radar

data to document polarimetric characteristics of the ML in 33 cold-season precipitation events with high vertical resolution and improved statistical accuracy. The heights of the ML top and ML bottom are determined using a ρ_{HV} threshold and then compared to those found by FZ95 who use a reflectivity-based curvature method. The curvature and polarimetric methods compare well within regions of higher Z_H , with the FZ95 curvature method exhibiting slightly higher (i.e., approximately 200 m) ML tops and slightly higher or lower (i.e., approximately 50 m) ML bottoms. Within regions of $Z_H < 20$ dBZ, the FZ95 method frequently failed. Using the QVPs, statistical

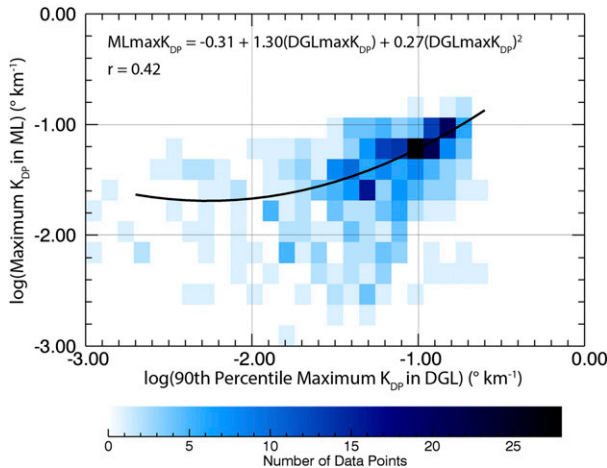


FIG. 13. Composite density scatterplot featuring a positive correlation ($r = 0.42$ for a quadratic fit) between $\log(90\text{th-percentile maximum } K_{DP} \text{ in the DGL})$ ($^{\circ} \text{ km}^{-1}$) and $\log(\text{maximum } K_{DP} \text{ in the ML})$ for the 33 QVP ML events (at S band).

relationships are developed to gain insight into the evolution of microphysical processes above, within, and below the ML, leading to a statistical polarimetric model of the ML that reveals characteristics that reflectivity data alone are not able to provide, particularly in regions of weak Z_H .

A significant and repetitive feature of the events studied is the occurrence of two ML regimes. Regions of higher Z_H distinctly indicate the presence and location of a ML collocated with enhanced Z_{DR} and reduced ρ_{hv} while at other times a well-defined ML is difficult to discern using Z_H alone (e.g., Fig. 1). During the periods of weak Z_H (i.e., <20 dBZ), the ML is only identifiable in the polarimetric imagery where a distinct ML signature is clearly evident in the Z_{DR} and ρ_{hv} fields. Furthermore, a nonmonotonic dependence of Z_{DR} on Z_H in the ML is observed. The evidence of very large Z_{DR} (up to 4 dB) and δ up to 8° associated with lower Z_H (from -10 to 20 dBZ) is documented when pristine, nonaggregated ice falls through the ML. When Z_H in the ML is large (i.e., >20 dBZ), a stronger relationship between Z_H and Z_{DR} in the ML is observed, as ice particles and aggregates become more oblate as they melt.

Another notable feature of the polarimetric QVP ML data are the values of δ observed at S band, generally ranging from -1° to 5° with maximum values up to 8° . The larger δ values are positively correlated with Z_{DR} in the ML and are observed not only within enhanced Z_H , but also in regions of weak Z_H , when a ML signature would not be detected using conventional Z_H data alone. Larger Z_{DR} in the ML generally occur with larger δ , potentially indicating more efficient aggregation

above the ML and larger-sized partially melted snowflakes in the ML. We also present the first QVP observations of K_{DP} in MLs at S band, which reveal positive correlation (i.e., $r = 0.57$) between maximum K_{DP} and maximum Z_H in the ML. This provides confidence in the QVP processing routine implemented for K_{DP} estimation in the ML. Results presented in the paper are also compared with those of a previously published study conducted at X band in Germany.

Analyses indicate positive correlation (i.e., 0.89 and 0.96, respectively) between Z_H in rain (i.e., 0.3 km below ML) and Z_H in snow (i.e., 0.3 km above ML) and between Z_H in rain and maximum Z_H in the ML. The correlation between these variables suggests that Z_H measurements in the ML can be used to estimate precipitation intensity near the surface in winter weather systems, where the height of the ML is typically quite low. Also, negative correlation occurs between minimum ρ_{hv} in the ML and the corresponding enhancement of Z_H (i.e., $\Delta Z_H = Z_{Hmax} - Z_{Hrain}$), with greater ΔZ_H generally associated with lower minimum ρ_{hv} in the ML. Positive correlation exists between maximum Z_{DR} in the ML and ΔZ_H , with greater Z_{DR} in the ML generally occurring during greater ΔZ_H . Also, greater ML depths occur during lower minimum ρ_{hv} and higher maximum Z_{DR} in the ML, with correlation between ML depth and minimum ρ_{hv} in the ML. These ML statistics are particularly important for developing a PVPR technique to mitigate the impact of ML contamination on polarimetric QPE.

A microphysically driven connection has been found between polarimetric signatures in the ML and aloft in the DGL and the temperature at the top of the cloud. Observations of high K_{DP} in the ML is typically associated with sagging bright bands during colder cloud-top temperatures, enhanced amount of snow above the ML, and enhanced K_{DP} in the dendritic growth layer (DGL; between -10° and -20°C). Also, a positive correlation (i.e., 0.42) between K_{DP} in the DGL and K_{DP} in the ML is observed.

Overall, the results of this analysis provide a next step toward advancing understanding of ML microphysical processes in cold-season precipitation and demonstrate the value and reliability of QVPs in detecting key features in ML regions of clouds. Considering that polarimetric radar variables in the ML are poorly represented in numerical weather prediction models, statistical analyses of polarimetric signatures in and near the ML such as those presented here have the potential to lead to improved model parameterizations as well as improved estimation of precipitation intensity near the surface in winter storms.

Acknowledgments. The authors thank John Krause and Pengfei Zhang for instrumental advice and coding assistance

in creating and improving the QVP plotting methodology. Funding was provided by the NOAA/Office of Oceanic and Atmospheric Research under NOAA–University of Oklahoma Cooperative Agreement NA16OAR4320115 (U.S. Department of Commerce) and by the U.S. National Weather Service, Federal Aviation Administration, and U.S. Department of Defense program for modernization of NEXRAD radars. Additional funding came from National Science Foundation Grant 1841246 and U.S. Department of Energy Grant DE-SC0008811.

REFERENCES

- Andrić, J., M. R. Kumjian, D. S. Zrnić, J. M. Straka, and V. M. Melnikov, 2013: Polarimetric signatures above the melting layer in winter storms: An observational and modeling study. *J. Appl. Meteor. Climatol.*, **52**, 682–700, <https://doi.org/10.1175/JAMC-D-12-028.1>.
- Balakrishnan, N., and D. S. Zrnić, 1990: Use of polarization to characterize precipitation and discriminate large hail. *J. Atmos. Sci.*, **47**, 1525–1540, [https://doi.org/10.1175/1520-0469\(1990\)047<1525:UOPTCP>2.0.CO;2](https://doi.org/10.1175/1520-0469(1990)047<1525:UOPTCP>2.0.CO;2).
- Bandera, J., A. D. Papatosoris, P. A. Watson, J. Tan, and J. W. Goddard, 1998: Method for detecting the extent of the melting layer. *IET Electron. Lett.*, **34**, 2104, <https://doi.org/10.1049/el:19981462>.
- Bechini, R., L. Baldini, and V. Chandrasekar, 2013: Polarimetric radar observations in the ice region of precipitating clouds at C-band and X-band radar frequencies. *J. Appl. Meteor. Climatol.*, **52**, 1147–1169, <https://doi.org/10.1175/JAMC-D-12-055.1>.
- Benjamin, S., and Coauthors, 2016: A North American hourly assimilation and model forecast cycle: The Rapid Refresh. *Mon. Wea. Rev.*, **144**, 1669–1694, <https://doi.org/10.1175/MWR-D-15-0242.1>.
- Boodoo, S., D. Hudak, N. Donaldson, and M. Leduc, 2010: Application of dual-polarization radar melting-layer detection algorithm. *J. Appl. Meteor. Climatol.*, **49**, 1779–1793, <https://doi.org/10.1175/2010JAMC2421.1>.
- Borowska, L., D. Zrnić, A. Ryzhkov, P. Zhang, and C. Simmer, 2011: Polarimetric estimates of a 1-month accumulation of light rain with a 3-cm wavelength radar. *J. Hydrometeorol.*, **12**, 1024–1039, <https://doi.org/10.1175/2011JHM1339.1>.
- Brandes, E., and K. Ikeda, 2004: Freezing-level estimation with polarimetric radar. *J. Appl. Meteor.*, **43**, 1541–1553, <https://doi.org/10.1175/JAM2155.1>.
- Bukovčić, P., A. V. Ryzhkov, D. Zrnić, and G. Zhang, 2018: Polarimetric radar relations for quantification of snow based on disdrometer data. *J. Appl. Meteor. Climatol.*, **57**, 103–120, <https://doi.org/10.1175/JAMC-D-17-0090.1>.
- Byers, H. R., and R. D. Coons, 1947: The ‘bright line’ in radar cloud echoes and its probable explanation. *J. Meteor.*, **4**, 78–81, [https://doi.org/10.1175/1520-0469\(1947\)004<0078:TLIRCE>2.0.CO;2](https://doi.org/10.1175/1520-0469(1947)004<0078:TLIRCE>2.0.CO;2).
- Carlin, J. T., and A. V. Ryzhkov, 2019: Estimation of melting-layer cooling rate from dual-polarization radar: Spectral bin model simulations. *J. Appl. Meteor. Climatol.*, **58**, 1485–1508, <https://doi.org/10.1175/JAMC-D-18-0343.1>.
- Durden, S. L., A. Kitiyakara, I. Eastwood, A. B. Tanner, Z. S. Haddad, F. K. Li, and W. J. Wilson, 1997: ARMAR observations of the melting layer during TOGA COARE. *IEEE Trans. Geosci. Remote Sens.*, **35**, 1453–1456, <https://doi.org/10.1109/36.649800>.
- Fabry, F., and I. Zawadzki, 1995: Long-term radar operations of the melting layer of precipitation and their interpretation. *J. Atmos. Sci.*, **52**, 838–851, [https://doi.org/10.1175/1520-0469\(1995\)052<0838:LTROOT>2.0.CO;2](https://doi.org/10.1175/1520-0469(1995)052<0838:LTROOT>2.0.CO;2).
- Fridlind, A. M., and Coauthors, 2017: Derivation of aerosol profiles for MC3E convection studies and use in simulations of the 20 May squall line case. *Atmos. Chem. Phys.*, **17**, 5947–5972, <https://doi.org/10.5194/acp-17-5947-2017>.
- Garvert, M. F., B. A. Colle, and C. F. Mass, 2005: The 13–14 December 2001 IMPROVE-2 event. Part I: Synoptic and mesoscale evolution and comparison with a mesoscale model simulation. *J. Atmos. Sci.*, **62**, 3474–3492, <https://doi.org/10.1175/JAS3549.1>.
- Giangrande, S. E., J. M. Krause, and A. V. Ryzhkov, 2008: Automated designation of the melting layer with a polarimetric prototype of the WSR-88D radar. *J. Appl. Meteor. Climatol.*, **47**, 1354–1364, <https://doi.org/10.1175/2007JAMC1634.1>.
- Gourley, J. J., and C. M. Calvert, 2003: Automated detection of the bright band using WSR-88D data. *Wea. Forecasting*, **18**, 585–599, [https://doi.org/10.1175/1520-0434\(2003\)018<0585:ADOTBB>2.0.CO;2](https://doi.org/10.1175/1520-0434(2003)018<0585:ADOTBB>2.0.CO;2).
- Griffin, E. M., T. J. Schuur, A. V. Ryzhkov, H. D. Reeves, and J. C. Picca, 2014: A polarimetric and microphysical investigation of the northeast blizzard of 8–9 February 2013. *Wea. Forecasting*, **29**, 1271–1294, <https://doi.org/10.1175/WAF-D-14-00056.1>.
- , —, and —, 2018: A polarimetric analysis of ice microphysical processes in snow, using quasi-vertical profiles. *J. Appl. Meteor. Climatol.*, **57**, 31–50, <https://doi.org/10.1175/JAMC-D-17-0033.1>.
- Hendry, A., Y. M. M. Antar, and G. C. McCormick, 1987: On the relationship between the degree of preferred orientation in precipitation and dual-polarization radar echo characteristics. *Radio Sci.*, **22**, 37–50, <https://doi.org/10.1029/RS022i001p00037>.
- Illingworth, A. J., and I. J. Caylor, 1989: Cross polar observations of the bright band. *24th Conf. on Radar Meteorology*, Tallahassee, FL, Amer. Meteor. Soc., 323–327.
- Kalogiros, J., M. N. Anagnostou, E. Anagnostou, M. Montopoli, E. Picciotti, and F. S. Marzano, 2013: Correction of polarimetric radar reflectivity measurements and rainfall estimates for apparent vertical profile in stratiform rain. *J. Appl. Meteor. Climatol.*, **52**, 1170–1186, <https://doi.org/10.1175/JAMC-D-12-0140.1>.
- Kennedy, P. C., and S. A. Rutledge, 2011: S-band dual-polarization radar observations of winter storms. *J. Appl. Meteor. Climatol.*, **50**, 844–858, <https://doi.org/10.1175/2010JAMC2558.1>.
- Kirstetter, P.-E., H. Andrieu, B. Boudevillain, and G. Delrieu, 2013: A physically based identification of vertical profiles of reflectivity from volume scan radar data. *J. Appl. Meteor. Climatol.*, **52**, 1645–1663, <https://doi.org/10.1175/JAMC-D-12-0228.1>.
- Kumjian, M. R., and K. A. Lombardo, 2017: Insights into the evolving microphysical and kinematic structure of northeastern U.S. winter storms from dual-polarization Doppler radar. *Mon. Wea. Rev.*, **145**, 1033–1061, <https://doi.org/10.1175/MWR-D-15-0451.1>.
- , A. V. Ryzhkov, H. D. Reeves, and T. J. Schuur, 2013: A dual polarization radar signature of hydrometeor refreezing in winter storms. *J. Appl. Meteor. Climatol.*, **52**, 2549–2566, <https://doi.org/10.1175/JAMC-D-12-0311.1>.
- , S. Mishra, S. E. Giangrande, T. Toto, A. V. Ryzhkov, and A. Bansemmer, 2016: Polarimetric radar and aircraft observations of saggy bright bands during MC3E. *J. Geophys. Res. Atmos.*, **121**, 3584–3607, <https://doi.org/10.1002/2015JD024446>.

- Lin, Y., and B. A. Colle, 2009: The 4–5 December 2001 IMPROVE-2 event: Observed microphysics and comparisons with the Weather Research and Forecasting Model. *Mon. Wea. Rev.*, **137**, 1372–1392, <https://doi.org/10.1175/2008MWR2653.1>.
- Matrosov, S. Y., R. F. Reinking, and I. V. Djalalova, 2005: Inferring fall attitudes of pristine dendritic crystals from polarimetric radar data. *J. Atmos. Sci.*, **62**, 241–250, <https://doi.org/10.1175/JAS-3356.1>.
- , K. A. Clar, and D. E. Kingsmill, 2007: A polarimetric radar approach to identify rain, melting layer, and snow regions for applying corrections to vertical profiles of reflectivity. *J. Appl. Meteor. Climatol.*, **46**, 154–166, <https://doi.org/10.1175/JAM2508.1>.
- Melnikov, A., 2012: Differential phase upon scattering by Rayleigh particles. *Seventh European Conf. on Radar in Meteorology and Hydrology*, Toulouse, France, Météo France, http://www.meteo.fr/cic/meetings/2012/ERAD/extended_abs/MIC_252_ext_abs.pdf.
- Melnikov, V., and J. M. Straka, 2013: Axis ratios and flutter angles of cloud ice particles: Retrievals from radar data. *J. Atmos. Oceanic Technol.*, **30**, 1691–1703, <https://doi.org/10.1175/JTECH-D-12-00212.1>.
- Melnikov, A., V. Melnikov, and A. V. Ryzhkov, 2005: On the differential phase in the melting layer. *33rd Conf. on Radar Meteorology*, Albuquerque, NM, Amer. Meteor. Soc., P9R.9, <https://ams.confex.com/ams/pdfpapers/95655.pdf>.
- Moisseev, D., E. Saltikoff, and M. Leskinen, 2009: Dual-polarization weather radar observations of snow growth processes. *34th Conf. on Radar Meteorology*, Williamsburg, VA, Amer. Meteor. Soc., 13B.2, <https://ams.confex.com/ams/pdfpapers/156123.pdf>.
- Ryzhkov, A. V., and D. Zrnić, 2019: *Radar Polarimetry for Weather Observations*. Springer, 486 pp.
- , D. S. Zrnić, and B. A. Gordon, 1998: Polarimetric method for ice water content determination. *J. Appl. Meteor.*, **37**, 125–134, [https://doi.org/10.1175/1520-0450\(1998\)037<0125:PMFIWC>2.0.CO;2](https://doi.org/10.1175/1520-0450(1998)037<0125:PMFIWC>2.0.CO;2).
- , S. E. Giangrande, and T. J. Schuur, 2005: Rainfall estimation with a polarimetric prototype of WSR-88D. *J. Appl. Meteor.*, **44**, 502–515, <https://doi.org/10.1175/JAM2213.1>.
- , P. Zhang, H. D. Reeves, M. R. Kumjian, T. Tschallener, S. Trömel, and C. Simmer, 2016: Quasi-vertical profiles—A new way to look at polarimetric radar data. *J. Atmos. Oceanic Technol.*, **33**, 551–562, <https://doi.org/10.1175/JTECH-D-15-0020.1>.
- , P. Bukovcic, A. Murphy, P. Zhang, and G. McFarquhar, 2018: Ice microphysical retrievals using polarimetric radar data. *10th European Conf. on Radar in Meteorology and Hydrology*, Netherlands, KNMI, 40, projects.knmi.nl/erad2018/ERAD2018_extended_abstract_040.pdf.
- Schrom, R. S., M. R. Kumjian, and Y. Lu, 2015: Polarimetric radar signatures of dendritic growth zones within Colorado winter storms. *J. Appl. Meteor. Climatol.*, **54**, 2365–2388, <https://doi.org/10.1175/JAMC-D-15-0004.1>.
- Smith, T. L., S. G. Benjamin, J. M. Brown, S. Weygandt, T. Smirnova, and B. Schwartz, 2008: Convection forecasts from the hourly updated, 3-km High Resolution Rapid Refresh (HRRR) model. *24th Conf. on Severe Local Storms*, Savannah, GA, Amer. Meteor. Soc., 11.1, <https://ams.confex.com/ams/pdfpapers/142055.pdf>.
- Stark, D., B. A. Colle, and S. E. Yuter, 2013: Observed microphysical evolution for two East Coast winter storms and the associated snow bands. *Mon. Wea. Rev.*, **141**, 2037–2057, <https://doi.org/10.1175/MWR-D-12-00276.1>.
- Stewart, R. E., 1992: Precipitation types in the transition region of winter storms. *Bull. Amer. Meteor. Soc.*, **73**, 287–296, [https://doi.org/10.1175/1520-0477\(1992\)073<0287:PTITTR>2.0.CO;2](https://doi.org/10.1175/1520-0477(1992)073<0287:PTITTR>2.0.CO;2).
- , J. D. Marwitz, and J. C. Pace, 1984: Characteristics through the melting layer of stratiform clouds. *J. Atmos. Sci.*, **41**, 3227–3237, [https://doi.org/10.1175/1520-0469\(1984\)041<3227:CTTMLO>2.0.CO;2](https://doi.org/10.1175/1520-0469(1984)041<3227:CTTMLO>2.0.CO;2).
- Straka, J. M., D. S. Zrnić, and A. V. Ryzhkov, 2000: Bulk hydrometeor classification and quantification using polarimetric radar data: Synthesis of relations. *J. Appl. Meteor.*, **39**, 1341–1372, [https://doi.org/10.1175/1520-0450\(2000\)039<1341:BHCAQU>2.0.CO;2](https://doi.org/10.1175/1520-0450(2000)039<1341:BHCAQU>2.0.CO;2).
- Tabary, P., A. Henaff, G. Vulpiani, J. Parent-du-Chatelet, and J. Gourley, 2006: Melting layer characterization and identification with a C-band dual-polarization radar: A long term analysis. *Fourth European Conf. on Radar in Meteorology and Hydrology (ERAD 2006)*, Barcelona, Spain, Servei Meteorològic de Catalunya, 17–20.
- Tobin, D. M., and M. R. Kumjian, 2017: Polarimetric radar and surface-based precipitation-type observations of ice pellet to freezing rain transitions. *Wea. Forecasting*, **32**, 2065–2082, <https://doi.org/10.1175/WAF-D-17-0054.1>.
- Trömel, S., M. R. Kumjian, A. V. Ryzhkov, C. Simmer, and M. Diederich, 2013: Backscatter differential phase—Estimation and variability. *J. Appl. Meteor. Climatol.*, **52**, 2529–2548, <https://doi.org/10.1175/JAMC-D-13-0124.1>.
- , A. V. Ryzhkov, P. Zhang, and C. Simmer, 2014: Investigations of the backscatter differential phase in the melting layer. *J. Appl. Meteor. Climatol.*, **53**, 2344–2359, <https://doi.org/10.1175/JAMC-D-14-0050.1>.
- , —, B. Hickman, and C. Simmer, 2017: Climatology of the vertical profiles of polarimetric radar variables at X band in stratiform clouds. *38th Conf. on Radar Meteorology*, Chicago, IL, Amer. Meteor. Soc., 5, <https://ams.confex.com/ams/38RADAR/webprogram/Paper320485.html>.
- , —, —, K. Muhlbauer, and C. Simmer, 2019: Polarimetric radar variables in the layers of melting and dendritic growth at X band—Implications for a nowcasting strategy in stratiform rain. *J. Appl. Meteor. Climatol.*, **58**, 2497–2522, <https://doi.org/10.1175/JAMC-D-19-0056.1>.
- Wolfensberger, D., D. Scipion, and A. Berne, 2015: Detection and characterization of the melting layer based on polarimetric radar scans. *Quart. J. Roy. Meteor. Soc.*, **142**, 108–124, <https://doi.org/10.1002/qj.2672>.
- Zrnić, D. S., N. Balakrishnan, C. L. Ziegler, V. N. Bringi, K. Aydin, and T. Matejka, 1993: Polarimetric signatures in the stratiform region of a mesoscale convective system. *J. Appl. Meteor.*, **32**, 678–693, [https://doi.org/10.1175/1520-0450\(1993\)032<0678:PSITSR>2.0.CO;2](https://doi.org/10.1175/1520-0450(1993)032<0678:PSITSR>2.0.CO;2).